Geophysical Journal International

Geophys. J. Int. (2013) **192,** 260–274 doi: 10.1093/gji/ggs011

Stress drop and source scaling of the 2009 April L'Aquila earthquakes

Giovanna Calderoni,[1] Antonio Rovelli[1] and Shri Krishna Singh[2]

[1]*Istituto Nazionale di Geofisica e Vulcanologia, Rome, Italy. E-mail: giovanna.calderoni@ingv.it*
[2]*Instituto de Geofísica, Universidad Nacional Autónoma de México, México D.F., Mexico*

Accepted 2012 October 5. Received 2011 September 23; in original form 2012 October 05

SUMMARY

The empirical Green's function (EGF) technique is applied in the frequency domain to 962 broad-band seismograms ($3.3 \leq M_W \leq 6.1$) to determine stress drop and source scaling of the 2009 April L'Aquila earthquakes. The station distance varies in the range 100–250 km from the source. Ground motions of several L'Aquila earthquakes are characterized by large azimuthal variations due to source directivity, even at low magnitudes. Thus, the individual-station stress-drop estimates are significantly biased when source directivity is not taken into account properly. To reduce the bias, we use single-station spectral ratios with pairs of earthquakes showing a similar degree of source directivity. The superiority of constant versus varying stress-drop models is assessed through minimization of misfit in a least-mean-square sense. For this analysis, seismograms of 26 earthquakes occurring within 10 km from the hypocentres of the three strongest shocks are used. We find that a source model where stress drop increases with the earthquake size has the minimum misfit: as compared to the best constant stress-drop model the improvement in the fit is of the order of 40 per cent. We also estimate the stress-drop scaling on a larger data set of 64 earthquakes, all of them having an independent estimate of seismic moment and consistent focal mechanism. An earthquake which shows no directivity is chosen as EGF event. This analysis confirms the former trend and yields individual-event stress drops very close to 10 MPa at magnitudes $M_W > 4.5$ that decrease to 1 MPa, on the average, at the smallest magnitudes. A varying stress-drop scaling of L'Aquila earthquakes is consistent with results from other studies using EGF techniques but contrasts with results of authors that used inversion techniques to separate source from site and propagation effects. We find that there is a systematic difference for small events between the results of the two methods, with lower and less scattered values of stress drop resulting from the EGF approach.

Key words: Earthquake ground motions; Body waves.

1 INTRODUCTION

The strong seismic activity in central Italy that struck the city of L'Aquila in 2009 April was characterized by three major ($M_W > 5.0$) normal-faulting earthquakes within 4 d (Chiarabba *et al.* 2009). The epicentres (star symbols) and focal mechanisms of these events are shown in Fig. 1. Rupture episodes were located in three different nearly collinear NW–SE to NNW–SSE striking faults. The occurrence of many significant shocks near the three major events with well-determined source mechanisms (Herrmann *et al.* 2011, indicated as HMM11 hereinafter) allows the application of the empirical Green's function (EGF) technique to study source scaling. In this paper, we apply the EGF technique to broad-band seismograms recorded in peninsular Italy by the permanent network operated by Istituto Nazionale di Geofisica e Vulcanologia (INGV). Stations in the epicentral distance range $100 < R < 250$ km were not clipped maintaining a good signal-to-noise ratio and are especially well suited for the purpose of this study.

Several papers have focussed on source scaling for the L'Aquila earthquakes, reaching different conclusions. Malagnini *et al.* (2011, indicated as MAL11 hereinafter) applied the EGF technique to coda waves of the strongest shocks, and a similar analysis has been extended recently to about 100 smaller magnitude earthquakes using time windows of *S* waves (Luca Malagnini 2012, personal communication). In these EGF-based estimates, the smaller events of the L'Aquila seismic sequence have lower stress drops as compared to the larger magnitude events, with a source scaling variation between small and large events. Other papers have used the generalized inversion technique (GIT) to separate source, crustal propagation and site terms. Bindi *et al.* (2009, indicated as BIN09 hereinafter) applied the GIT to the accelerograms of 13 of the strongest L'Aquila earthquakes and inferred a substantially constant stress-drop trend. Similarly, Ameri *et al.* (2011, indicated as AME11 hereinafter) applied the GIT technique to about 100 aftershocks in the magnitude range $3.1 < M_L < 5.3$ and concluded that the fluctuation of individual-earthquake stress drop is large ($0.1 < \Delta\sigma < 60$ MPa)

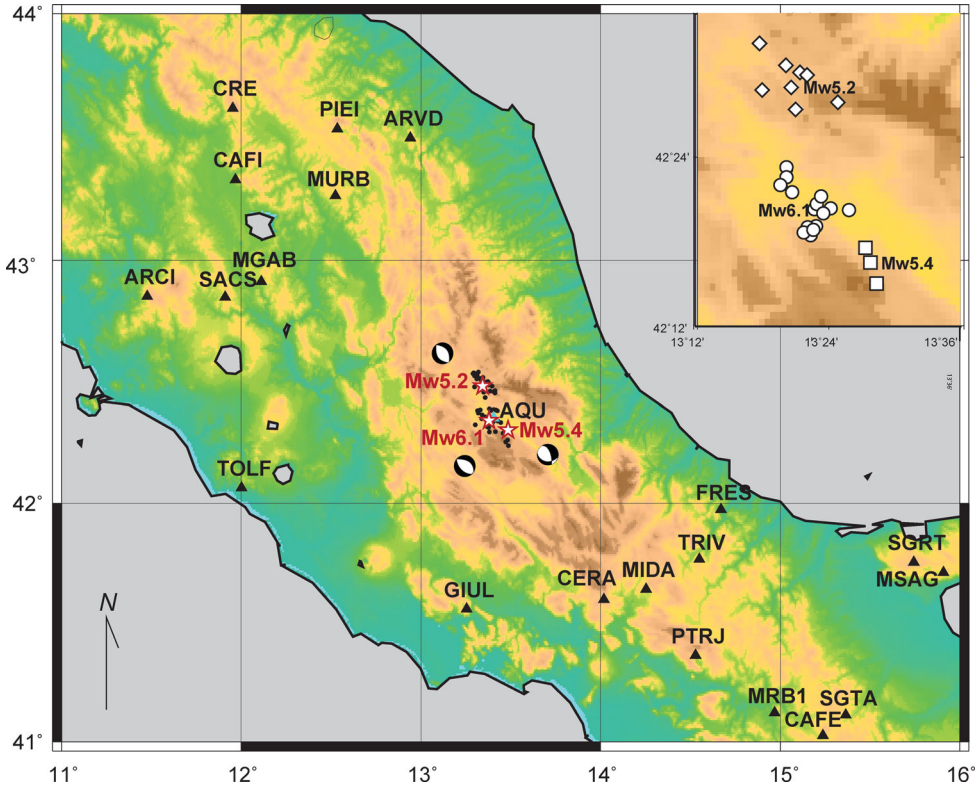

Figure 1. Map of the study area. Permanent broad-band stations used in the analysis are indicated by black triangles, the star symbols are the epicentres of the three largest shocks of the L'Aquila seismic sequence and black dots are 61 of the smaller earthquakes analysed in this study. The fault plane solutions are taken from Herrmann *et al.* (2011). The inset shows three clusters of events resulting from three strongest shocks during the L'Aquila sequence. Events in each cluster are analysed separately using the EGF technique.

but independent of source size. We think that the EGF technique is more efficient in eliminating the role of path and site effects than GIT and can yield more reliable estimates especially when, as in the case of L'Aquila earthquakes, a good control on focal mechanism and seismic moment is available from HMM11. In contrast, BIN09 discussed the difficulties of their approach in using the same propagation model for small (20–30 km) and intermediate (≈100 km) distances and some discrepancies in the site-effect assessment for different events at near-source stations. Here we employ a combination of data (broad-band velocity-transducer seismograms) and technique (single-station spectral ratios by windowing *S* waves and early coda) not used so far in the analysis of the L'Aquila earthquakes.

A key feature of this study is the azimuthal dependence of spectral amplitudes caused by source directivity, even at small magnitudes, and its effect on stress-drop estimates. The rupture directivity of the L'Aquila main shock is discussed by Cirella *et al.* (2009, 2012) and Pino & Di Luccio (2009), and its significant effect on ground motions up to large distances in Italy is documented by several authors (Akinci *et al.* 2010; Çelebi *et al.* 2010; Di Alessandro *et al.* 2012). Rupture directivity is expected to cause an azimuthal variation of amplitude and shaking duration resulting in higher corner frequency (and, hence, larger stress drop) at stations in the direction of rupture propagation as compared to stations in the opposite direction. The source directivity even for small magnitudes has been observed for many earthquakes in California (Boatwright 2007; Seekins & Boatwright 2010; Lengliné & Got 2011). In this paper we demonstrate that source directivity was also significant for many of the smaller shocks of the L'Aquila seismic sequence.

The goals of this study are (i) to identify events of the seismic sequence that are characterized by strong source directivity and require special care to minimize errors in the estimated stress drops, (ii) to derive a stress-drop scaling relation affected as little as possible by source directivity and (iii) to compare the different scaling laws proposed in the literature for the L'Aquila earthquakes and discuss the origin of differences and statistical uncertainties. We find that the dispersion of individual-event stress-drop estimates seems to be better controlled in our approach compared to the GIT estimates because of our use of independent (long-period) estimates of seismic moment, and the greater EGF efficiency in separating source from propagation terms. Our results depict a well-constrained trend of stress drops that decreases at smaller magnitudes (by one decade over four decades of seismic moment), confirming the same value (≈ 10 MPa) of the largest magnitude earthquakes found by other authors. This study leads to the same conclusion as many others using EGF technique (e.g. Abercrombie & Rice 2005; Mayeda *et al.* 2007; Malagnini *et al.* 2008; Calderoni *et al.* 2010): a breakdown of self-similarity between large- and small-size earthquakes.

2 DATA

The 2009 April 6 destructive event at 01:53 UTC near L'Aquila was followed by two other $M_W > 5.0$ earthquakes on April 7 and 9 which occurred southeast and northwest of the fault plane that ruptured during the main shock. The three strongest events are shown by the star symbol in Fig. 1. In this figure, the moment magnitudes and focal mechanisms are taken from the moment tensor solutions reported in HMM11. We note that the use of a local

Table 1. Earthquakes, grouped in three clusters (Fig. 1), selected to determine source scaling law.

Cluster	Event	Date 2009	Time, UTC	Lat N (°)	Long E (°)	Depth (km)	M_0 (N·m)	M_W
Cluster 1	1	March 30	1338	42.321	13.376	9.8	1.66×10^{15}	4.08
	2	March 30	2157	42.316	13.375	9.5	1.93×10^{14}	3.46
	3	April 5	2048	42.325	13.382	9.5	9.55×10^{14}	3.92
	4	April 6	0132	42.342	13.380	8.3	1.97×10^{18}	6.13
	5	April 6	0227	42.374	13.342	8.3	1.78×10^{15}	4.10
	6	April 6	0237	42.366	13.334	8.7	2.07×10^{16}	4.81
	7	April 6	0621	42.341	13.427	8.8	2.54×10^{14}	3.54
	8	April 6	1036	42.343	13.402	9.9	1.20×10^{14}	3.31
	9	April 6	1414	42.359	13.350	9.7	2.37×10^{14}	3.52
	10	April 6	2156	42.384	13.342	10.0	6.10×10^{14}	3.79
	11	April 8	1034	42.347	13.383	9.3	1.99×10^{14}	3.47
	12	April 9	0931	42.355	13.389	8.8	8.41×10^{13}	3.22
	13	April 21	1544	42.324	13.371	10.0	2.45×10^{14}	3.53
	14	July 3	0114	42.319	13.366	11.1	2.06×10^{14}	3.48
	15	July 12	2214	42.338	13.392	11.1	4.41×10^{14}	3.70
Cluster 2	16	April 7	1747	42.275	13.464	17.1	1.70×10^{17}	5.42
	17	April 24	0436	42.254	13.472	8.5	9.66×10^{13}	3.26
	18	April 25	0208	42.290	13.457	8.9	8.41×10^{13}	3.22
Cluster 3	19	April 8	2256	42.497	13.367	10.8	7.76×10^{14}	3.86
	20	April 9	0052	42.484	13.343	11.0	8.51×10^{16}	5.22
	21	April 9	0341	42.507	13.337	10.7	7.85×10^{13}	3.20
	22	April 9	1938	42.501	13.356	9.3	3.72×10^{16}	4.98
	23	April 9	2240	42.480	13.298	11.1	4.62×10^{14}	3.71
	24	April 10	0322	42.465	13.414	9.6	5.13×10^{14}	3.74
	25	April 10	0433	42.458	13.350	11.2	1.29×10^{14}	3.34
	26	April 14	1928	42.535	13.294	10.0	1.32×10^{14}	3.35

velocity profile in HMM11 leads to a slight underestimation of the HMM11 seismic moments compared to those listed in the Global CMT catalogue (http://www.globalcmt.org). We prefer the values of HMM11 because they better fit the ground motion amplitudes at Italian broad-band stations in the intermediate-period range, 1–20 s (see also Scognamiglio *et al.* 2010), and yield results that are much more consistent with observations at low frequency, below $f \approx 1$ Hz. For the main shock, M_W is 6.1 as compared to 6.3 of the Global CMT catalogue; similarly M_W of April 7 and 9 earthquakes are 5.4 and 5.2 instead of 5.6 and 5.4. In any case, we have carefully checked that such differences in magnitude would not, in itself, be the cause of the difference in the source scaling between this study and others, which used different M_W values.

Since the basic assumption for the application of the EGF technique is that source locations and focal mechanisms of the events must be similar, we have used the catalogue of moment tensors by HMM11 to select smaller shocks having a consistent normal-faulting mechanism and hypocentres as close as possible to the three largest shocks. We have used stations in the distance range 100–250 km; the lower value of this range is sufficiently large for the point-source approximation to be valid and the upper value provides a satisfactory signal-to-noise ratio in the records down to magnitudes of the order of 3. The frequency bandwidth reduction at these distances and its potential limitation in the stress-drop estimation are discussed in the Appendix.

In the first part of our analysis, we have selected smaller shocks within a source distance of no more than 10 km from the three main shocks. Hypocentre determinations are taken from the INGV bulletin (http://iside.rm.ingv.it/iside). Earthquakes that satisfy this condition are listed in Table 1, subdivided into three clusters. Their epicentres are shown in the inset of Fig. 1 with different symbols for each cluster. For Cluster 1, 14 aftershocks are selected (open circles). For the M_W 5.4 shock of April 7 (event #16) only two aftershocks (open squares) were identified as valid EGFs, so Cluster 2 is composed of three events only. Cluster 3 (from # 19 to 25 in Table 1) contains earthquakes belonging to the Campotosto seismic sequence, about 20 km to the northwest of L'Aquila. It consists of seven aftershocks of the April 9 M_W 5.2 event (# 20) represented by open diamonds in the inset of Fig. 1.

Distance between main shock and EGF is generally less than 10 wavelengths at high frequency (about 6 km at 5 Hz). However, the maximum of 10 km separation between events is less than one-tenth of source-to-receiver distance, in rough agreement with the assumption that the propagation path does not differ between target events and EGFs.

In the second part of the analysis, we have applied the EGF technique to the entire seismic sequence, interdistance between events being one order of magnitude smaller than source-to-receiver distance. This allows us to assess the stress-drop scaling over a much larger number of events (a total of 64 earthquakes, listed in Table 2), all with fairly well-controlled focal mechanisms and seismic moments from HMM11 (black dots in Fig. 1).

Processed signals are broad-band seismograms recorded by velocity-transducer sensors (mostly Nanometrics Trillium 40-s). The instrumental correction of seismograms is performed using the factory supplied zeros and poles of the transfer function. The corrected velocity time-series are bandpass filtered between 0.1 and 20 Hz.

3 THE METHOD OF ANALYSIS

We follow the procedure outlined by Calderoni *et al.* (2010). Fourier amplitude spectrum of the recorded velocity time-series is written as

$$V(f, R) = \Omega_0(f) \cdot (2\pi f) \cdot P(f, R) \cdot H(f) \,. \quad (1)$$

Table 2. Earthquakes used in estimating stress-drop ratios and individual-event stress drops applying the EGF technique.

N		Time UTC	Lat (°)	Lon (°)	Dep (km)	M_W	$\Delta\sigma$ ((MPa)
1	30/03/2009	13:38	42. 321	13. 376	9.8	4.08	2.02
2	30/03/2009	13:43	42. 315	13. 378	9.7	3.53	1.86
3	30/03/2009	21:57	42. 316	13. 375	9.5	3.46	0.67
4	05/04/2009	20:48	42.325	13.382	9.5	3.92	4.45
5	05/04/2009	22:39	42.329	13.385	10.0	3.47	1.50
6	06/04/2009	01:32	42. 342	13. 380	8.3	6.13	9.11
7	06/04/2009	02:27	42. 374	13. 342	8.3	4.10	1.33
8	06/04/2009	02:37	42. 366	13. 334	8.7	4.81	3.54
9	10/04/2009	03:56	42. 335	13. 386	9.3	4.26	2.16
10	06/04/2009	04:47	42. 356	13.356	9.1	3.82	0.51
11	06/04/2009	06:21	42. 341	13.427	7.1	3.54	1.33
12	06/04/2009	06:48	42. 296	13.338	7.4	3.25	0.52
13	06/04/2009	10:36	42. 338	13. 402	9.9	3.31	1.49
14	06/04/2009	14:14	42.359	13. 350	9.7	3.52	0.48
15	06/04/2009	17:40	42. 384	13. 315	11.0	3.37	0.67
16	06/04/2009	21:56	42. 384	13. 342	10.0	3.79	1.60
17	06/04/2009	22:47	42. 326	13. 303	10.2	3.60	2.46
18	06/04/2009	23:15	42. 463	13. 385	9.7	4.90	5.56
19	07/04/2009	01:52	42. 460	13. 406	9.0	3.30	0.56
20	07/04/2009	12:29	42. 455	13. 413	8.7	3.59	1.26
21	07/04/2009	17:47	42. 303	13. 486	17.1	5.42	16.6
22	08/04/2009	10:34	42. 347	13. 383	9.3	3.47	0.95
23	08/04/2009	22:56	42. 497	13. 367	10.8	3.86	5.40
24	08/04/2009	23:18	42. 386	13. 331	11. 0	3.50	0.85
25	09/04/2009	00:52	42. 489	13. 351	11.0	5.22	11.5
26	09/04/2009	03:14	42. 335	13. 444	17.1	4.20	2.93
27	09/04/2009	03:41	42. 507	13. 337	10.7	3.20	4.46
28	09/04/2009	04:43	42. 502	13. 373	9.6	3.69	3.90
29	09/04/2009	09:31	42. 355	13. 389	8.8	3.22	1.06
30	09/04/2009	19:38	42. 504	13. 350	9.3	4.98	9.81
31	09/04/2009	22:40	42. 480	13. 298	11.1	3.71	2.06
32	10/04/2009	03:22	42. 465	13. 414	9.6	3.74	2.56
33	10/04/2009	04:33	42. 458	13. 350	11.2	3.34	2.63
34	10/04/2009	11:53	42. 239	13. 487	9.5	3.32	1.90
35	11/04/2009	05:39	42. 386	13. 418	10.6	3.44	3.56
36	11/04/2009	06:57	42. 388	13. 405	9.8	3.26	1.79
37	12/04/2009	18:05	42. 384	13. 388	8.9	3.21	1.31
38	12/04/2009	22:14	42. 338	13. 392	11.1	3.70	1. 88
39	13/04/2009	07:08	42. 262	13. 483	9.4	3.23	0.80
40	13/04/2009	21:14	42. 498	13. 377	9. 0	4.85	6.09
41	14/04/2009	13:56	42. 542	13. 320	9.9	3.84	2.91
42	14/04/2009	17:27	42. 528	13. 313	7.0	3.75	3.70
43	14/04/2009	19:28	42. 535	13. 294	10.0	3.35	2.33
44	14/04/2009	20:17	42. 526	13. 298	10.3	3.79	9.28
45	14/04/2009	20:53	42. 538	13. 294	10.2	3.28	1.56
46	15/04/2009	19:36	42. 514	13. 312	10.1	3.41	1.30
47	15/04/2009	22:53	42. 515	13. 330	9.0	3.86	3.09
48	16/04/2009	05:44	42. 297	13. 416	10.2	3.39	1.26
49	16/04/2009	17:49	42. 535	13. 291	11.5	3.76	6.51
50	18/04/2009	09:05	42. 436	13. 359	14.5	3.71	5.15
51	21/04/2009	15:44	42. 324	13. 371	10.0	3.53	1.44
52	24/04/2009	04:36	42. 254	13. 472	8.5	3.26	0.41
53	24/04/2009	13:38	42. 519	13. 345	8.9	3.23	2.09
54	25/04/2009	02:08	42. 290	13. 457	8.9	3.22	1.39
55	30/04/2009	13:01	42. 358	13. 358	10.5	3.52	0.89
56	03/05/2009	05:14	42. 360	13. 384	9.8	3.27	0.95
57	11/05/2009	16:59	42. 489	13. 377	9.7	3.25	2.37
58	14/05/2009	06:30	42. 483	13. 397	9.5	3.50	2.87
59	30/05/2009	02:55	42. 350	13. 339	11.0	3.57	1.23
60	03/07/2009	01:14	42. 319	13. 366	11.1	3.48	3.48
61	03/07/2009	09:43	42. 323	13. 375	10.3	3.43	2.11
62	03/07/2009	11:03	42. 391	13. 382	9.6	3.68	5.74
63	12/07/2009	08:38	42. 328	13. 379	10.1	4.09	2.33
64	12/07/2009	22:14	42. 338	13. 392	11.1	3.70	1.88

It represents the convolution of source, propagation in the crust and site transfer function [$\Omega_0(f)$, $P(f,R)$ and $H(f)$, respectively]. Following Brune (1970, 1971), the source-radiated displacement spectrum in the point-source approximation is expressed as

$$\Omega_0(f) = \frac{F_S R_{\vartheta,\phi}}{4\pi\rho\beta^3} \frac{M_0}{1+(f/f_0)^2}, \tag{2}$$

where M_0 and f_0 are seismic moment and corner frequency, respectively. F_S accounts for the free-surface effect (taken here as 2), $R_{\vartheta,\phi}$ is the radiation pattern, ρ is the density and β is the shear wave velocity in the source volume. For a circular crack with a uniform stress drop in an infinite Poisson solid, $\Delta\sigma$ is linked to M_0 and f_0 (Eshelby 1957; Keilis-Borok 1959; Brune 1970) through the relations

$$\Delta\sigma = \frac{7}{16}\frac{M_0}{r^3}, \tag{3}$$

$$r = \frac{2.34\beta}{2\pi f_0}, \tag{4}$$

where r is the radius of the fault.

The advantage of the single-station spectral ratio method is that the knowledge of propagation and site terms is not needed. When two earthquakes having different magnitude M_1 and M_2 are recorded at the same station, the ratio of their spectra

$$\frac{V_{M_1}(f)}{V_{M_2}(f)} = \frac{\Omega_{0,M_1}(f)P(f,R)H(f)}{\Omega_{0,M_2}(f)P(f,R)H(f)} = \frac{M_{0,M_1}}{M_{0,M_2}} \cdot \frac{1+(f/f_{0,M_2})^2}{1+(f/f_{0,M_1})^2} \tag{5}$$

reduces to the ratio of the two source terms since $P(f,R)$, and $H(f)$ are the same. When f_0 is written in terms of $\Delta\sigma$ and M_0 through (3) and (4), the application of eq. (5) requires the knowledge of a single propagation parameter (shear wave velocity β at the source depth, which appears in eq. 4). We use $\beta = 3.1$ km s^{-1} in accordance with the 1-D model (nnCIA.mod) inverted by HMM11. This value is consistent with the crust rigidity used in the seismic moment computation. As remarked by Ben-Zion (2001), seismic moment estimates are affected by uncertainties in the elastic moduli assumed to characterize source regions in different seismogenic areas. The seismic potency (or geometric moment) would be a more suitable parameter to measure earthquake sizes, with the evident advantage of not being affected by the assumed values of the poorly constrained crustal rigidity. However, for the sake of continuity with previous papers, we adopted the seismic moment scale.

Eq. (5) is controlled by the ratio of M_0 at low frequency and by the ratio of ${M_0}^{1/3} \cdot \Delta\sigma^{2/3}$ at high frequency. Since the values of M_0 are derived from independent estimates, $\Delta\sigma$ is the only unknown parameter. The spectral ratio (5) can be applied to pairs of different magnitude events to check if ground motion follows a constant or varying stress-drop scaling. In the Supporting Information (Fig. S1, panel a), we illustrate how the high-frequency asymptote of spectral ratios (5) gives insights on the stress-drop scaling.

In this paper, the most appropriate scaling model for the L'Aquila earthquakes is first searched through the best fit of observed spectral ratios over an extended magnitude range. *A priori*, a power-law relation between $\Delta\sigma$ and M_0 is assumed according to the equation

$$\log\Delta\sigma = p\log M_0 + q. \tag{6}$$

A linear relation between the logarithmic values of $\Delta\sigma$ and M_0 is typically used in scaling studies (e.g. a similar formalism is used in Candela *et al.* 2011) and its validity here is confirmed *a posteriori*. The appropriateness of the constant ($p = 0$) or varying stress-drop model ($p \neq 0$) is decided through the misfit

$$\varepsilon = \frac{1}{M}\sum_{m=1,M}\sqrt{\frac{\int_{f_{\min}}^{f_{\max}}(\log \mathrm{Obs}_m(f) - \log \mathrm{Theo}_m(f))^2\,\mathrm{d}f}{(f_{\max}-f_{\min})}}, \tag{7}$$

where $\mathrm{Obs_m}(f)$ are the empirical spectral ratios calculated from pairs of events with different magnitudes and $\mathrm{Theo_m}(f)$ are the corresponding mathematical functions (5) that are written in terms of M_0, p and q. M is the number of the spectral ratios curves used in the fit, and $f_{\min}$ and $f_{\max}$ are the lower and upper bounds of the frequency band of analysis (0.5 and 8 Hz, respectively, as described in detail in the Appendix). Spectral ratios are computed through FFT of 50 s time windows bracketing the most significant part (S waves and early coda) of the two horizontal components of corrected velocities. Windowing is made through the conventional Hanning taper of the SAC software, the spectra are smoothed with a 0.5-Hz-wide triangular operator of the same package (Goldstein *et al.* 2003). The geometric mean of the two horizontal components is computed for each record. Before the systematic spectral ratio analysis, the role of source directivity on ground motion spectra is checked.

4 DIRECTIVITY IN THE SOURCE SPECTRA OF L'AQUILA EARTHQUAKES

Source directivity during the April 6 main shock is well established. The large fault-transverse displacement pulses at near-source stations have been attributed to up-dip source directivity by Chioccarelli & Iervolino (2010). Their interpretation is consistent with the slip release as modelled by Cirella *et al.* (2009, 2012) who inferred up-dip rupture propagation from the nucleation point followed by rupture propagation from northwest to southeast along the fault strike. The along-strike directivity effect is very evident in the main shock accelerograms at farther stations which show strong azimuthal variation in peak ground motions (Akinci *et al.* 2010; Çelebi *et al.* 2010; Di Alessandro *et al.* 2012): stations southeast of the epicentre have systematically larger accelerations than those to the northwest.

Before proceeding to assess source scaling through (7), we investigate the role of source directivity on the Fourier amplitude spectra and spectral ratios using broad-band seismograms of several representative events (Fig. 2). Because of the influence of source directivity, an increase in the corner frequency, f_0, at stations in the direction of rupture, a decrease in opposite direction and a null effect in the orthogonal direction, is expected (see panel b of Fig. S1). To visualize f_0 variations as a function of azimuth, the Fourier amplitude spectra of acceleration are computed. The Fourier acceleration spectra are then scaled to unitary distance using the following three steps: (i) Correction of geometrical spreading ($1/R$). (ii) Compensation of high-frequency dissipation through the exponential function $e^{\pi\kappa f}$ (see Singh *et al.* 1982; Anderson & Hough 1984), where κ is a constant parameter of each station. For each station the geometric mean of κ was computed over the ensemble of the $M_W > 5$ earthquakes. The details are shown in the Supporting Information (Fig. S2). (iii) Computing seismic wave amplification in the crust and correcting acceleration spectra for this effect. The correction function is estimated following Boore (1986) using the velocity model nnCIA.mod by HMM11. The steps (i)–(iii) are used to compute the propagation terms $P(f,R)$ and $H(f)$ that appear in eq. (1). Further details can be found in Calderoni *et al.* (2010).

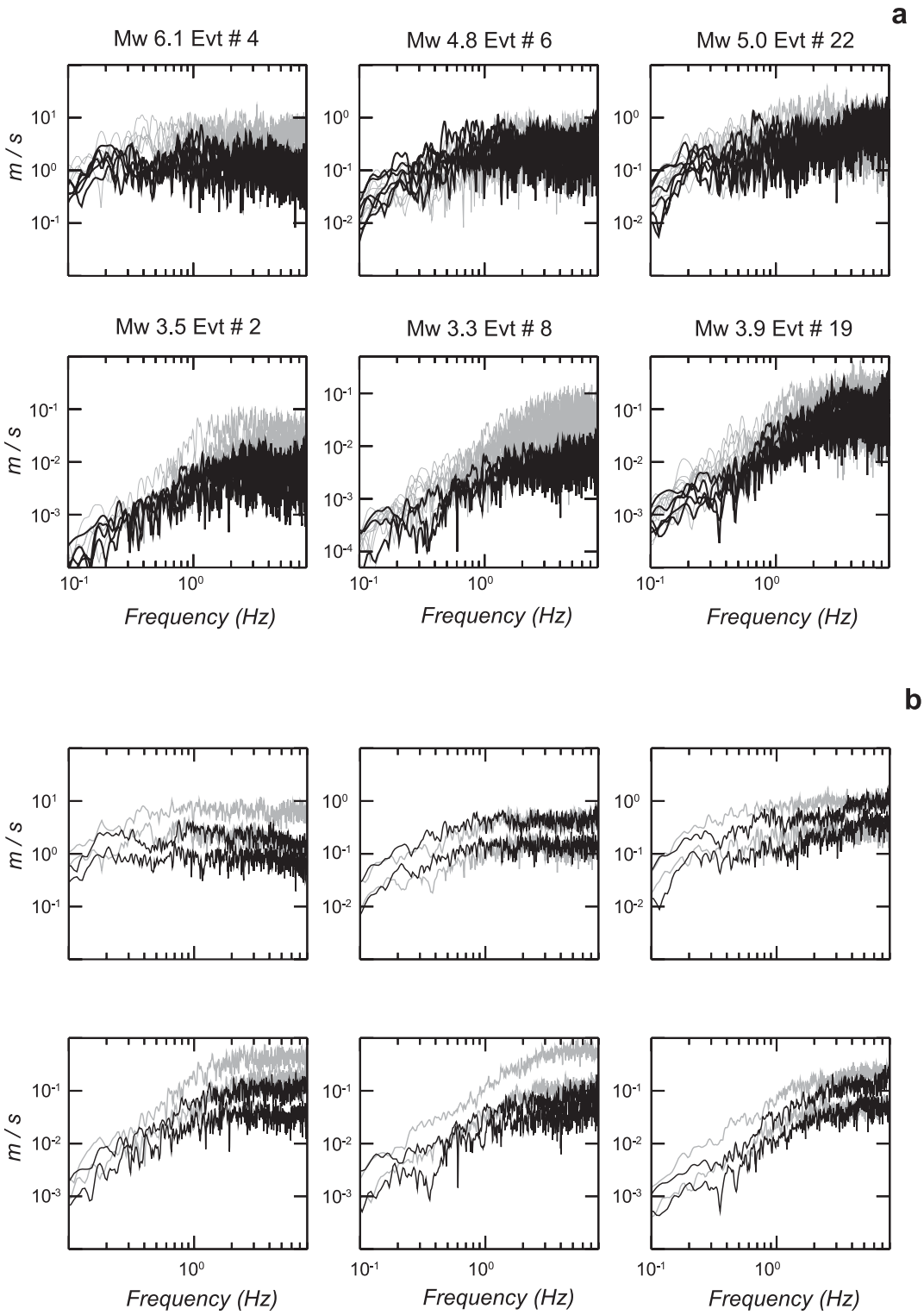

Figure 2. (a) Examples of acceleration spectra at different stations scaled to unitary distance. Black and grey curves represent spectra at stations to the NW and SE of the epicentres, respectively. (b) Same as panel (a) but showing the ±1 *SD* bands around geometric mean for NW and SE stations.

Fig. 2 shows the resulting scaled spectra of six representative events. The stations to the southeast and northwest are plotted as grey and black curves, respectively. The four curves in each panel of Fig. 2(b) represent the ±1 *SD* intervals around the geometric mean of the scaled spectra at stations to the northwest and southeast of epicentres. We note that, in some cases, the ±1 *SD* bands of the spectra show no or very partial overlap. In principle, both source directivity and propagation could be responsible for a strong azimuthal difference. However, a propagation effect should be common to all events for a given range of azimuths, and then it should be repeatedly observed for earthquakes having such close hypocentres. Therefore, along-strike source directivity is to be identified as

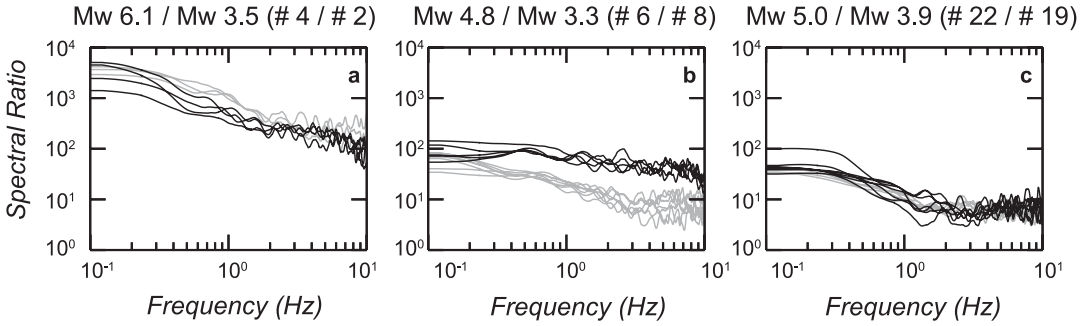

Figure 3. Spectral ratios for pairs of earthquakes whose spectra are shown in Fig. 2. Black and grey curves represent stations to the NW and SE of the epicentres, respectively. Each pair is chosen such that (a) both earthquakes exhibit strong directivity, (b) one with weak or no directivity and the other with strong directivity and (c) both with weak or no directivity.

the basic cause for the observed amplitude variation in the unitary-distance scaled spectra between stations northwest and southeast of the epicentres.

The source directivity during the April 6 main shock (event # 4) towards southeast is evident in Fig. 2(a, top panel, left frame) as the grey spectral curves corresponding to southeast stations are much higher than the black ones for the northwest stations. In contrast, event #22 (M_W 5.0), one of the earthquakes of the Campotosto group (top panel, right frame), shows no significant separation at high frequency among the spectra at stations in the opposite direction. This is indicative of bilateral rupture or weak directivity. Interestingly, Fig. 2 shows strong directivity for low-magnitude earthquakes also, for example, events # 2 and 8 (M_W 3.5 and 3.3, respectively). As mentioned earlier, the source directivity of small earthquakes has previously been reported by Boatwright (2007), Seekins & Boatwright (2010) and Lengliné & Got (2011).

Fig. 3 illustrates spectral ratios for pairs of earthquakes whose spectra are shown in Fig. 2. The pair of earthquakes is chosen such that (i) both exhibit strong directivity (event # 4/event #2, Fig. 3a), (ii) one with weak or no directivity and the other with strong directivity (event # 6/event #8, Fig. 3b) and (iii) both with weak or no directivity (event # 22/event # 19, Fig. 3c). As expected, the spectral-ratio curves of event pairs with similarly weak directivity have small dispersion (Fig. 3a). In fact, the spectral ratios at southeast stations (grey curves) overlap with those at northwest stations (black curves). This also occurs when there is strong directivity in both numerator and denominator events (details are discussed in Fig. S3). In contrast, the spectral ratios of pairs of events with distinct directivity are well separated at southeast and northwest stations, showing a difference of more than 10 at high frequencies (Fig. 3b). As illustrated in the Supporting Information (Figs S1 and S3), in the Brune (1970) model the high-frequency asymptote of the spectral ratio is controlled by the ratio of the product $M_0^{1/3} \cdot \Delta\sigma^{2/3}$. Thus, if the spectral ratios in Fig. 3(b) are interpreted in terms of this model, then apparent variations of stress drop could be as large as a factor of 5 due to source directivity. In a strict sense, Brune's model, in which the rupture is instantaneous over a circular fault, is reasonable only for the case shown in Fig. 3(c). This is because neither the spectra of event # 22 in the numerator nor those of event # 19 in the denominator reveal significant directivity. In Fig. 3(b) we show the increase in the variability of the high-frequency trend caused by the azimuthal variation of f_0 due to source directivity. In the Supporting Information (Fig. S3) we further discuss why the shift of f_0 has a small effect on the $\Delta\sigma$ estimate when both numerator and denominator events have a similar (even if strong) source directivity. Moreover, we demonstrate that an average over stations (equally distributed in azimuth) yields a valid estimate of $\Delta\sigma$ of individual event when an EGF with no directivity is used (Fig. S4). Of course, $\Delta\sigma$ estimates of events with strong source directivity will have a much larger standard deviation than events with weak directivity.

5 SEARCHING FOR THE BEST SCALING MODEL

5.1 Trends inferred from selected EGFs

To check the sensitivity of (5) in determining the source scaling we first studied the stability of the best-fit parameters p and q as defined in (6) when pairs of events with and without directivity are grouped separately. For Cluster 1 the spectral ratios were computed for 13 pairs, eight exhibiting strong directivity (a total of 64 spectral ratios, as listed in Table 3), and the other five showing small or no directivity (42 spectral ratios). Examples of spectral ratios with and without source directivity are shown in Figs 4(a) and (b) along with the best-fit curves computed through eq. (6) for the two groups of events separately and the corresponding values of p and q. When all the selected pairs of Cluster 1 (106 spectral ratios) are merged together, then the resulting best-fitting parameters are

$$\begin{aligned} p &= 0.24 \\ q &= -3.6, \end{aligned} \tag{8}$$

which differ by less than 6 per cent from the ones obtained for the two groups separately (Fig. 5a). In all cases, the parameters indicate a deviation from self-similarity, their slope predicting a variation of $\Delta\sigma$ by one order of magnitude over about four decades of seismic moments. To estimate the size of statistical fluctuations of the sample, a bootstrap analysis is applied later. The resulting estimated statistical uncertainty band is represented in Fig. 5(b) by the shaded area. We note that the two solutions of (6) using pairs of Cluster 1 with similar (strong and weak) directivity fall largely within statistical errors and follow the same trend. We note that even relatively few (of the order of five) pairs of events yield a sufficiently stable result when grouped consistently in terms of source directivity. This suggests that scatter in source scaling parameters is small when tens of spectral ratios are used and testifies to the efficacy of the EGF method in the frequency domain in capturing the mean scaling trend even when using a limited subset of data, provided that there is a reliable control on focal mechanisms and hypocentre locations, and independent long-period estimates of M_0 are available. The analysis also emphasizes the need for similar source directivity of the target

Table 3. Earthquake pair combinations for each cluster used in computing spectral ratios and establishing source scaling law.

	Numerator	Denominator	Strong directivity	Weak directivity
Cluster 1	#4	#2	#4/#2 (8)	
		#7	#4/#7 (10)	
		#8	#4/#8 (7)	
		#10	#4/#10 (8)	
		#11	#4/#11 (7)	
		#12	#4/#12 (6)	
		#13	#4/#13 (8)	
		#14	#4/#14 (10)	
	#6	#1		#6#1 (8)
		#3		#6/#3 (8)
		#5		#6/#5 (9)
		#9		#6/#9 (7)
		#15		#6/#15 (10)
Cluster 2	#16	#17	#16/#17 (3)	
		#18	#16/#18 (4)	
Cluster 3	#20	#21	#20/#21 (12)	
		#24	#20/#24 (16)	
		#25	#20/#25 (15)	
	#22	#19		#22/#19 (14)
		#23		#22/#23 (14)
		#26		#22/#26 (13)

Note: The number in the bracket refers to number of spectral ratios.

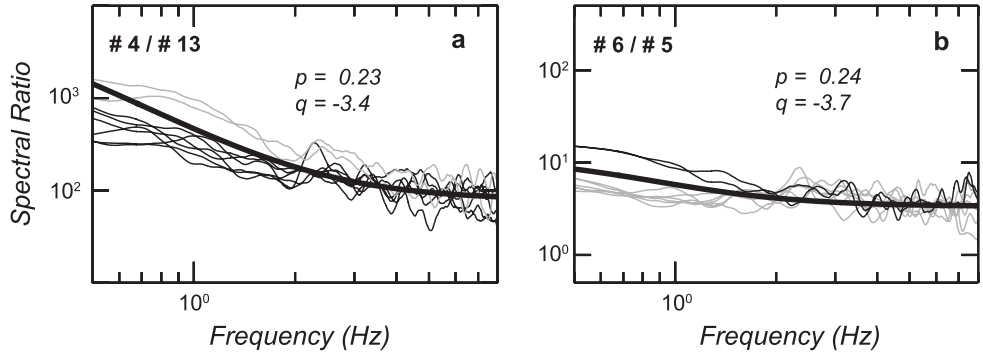

Figure 4. Examples of individual-station spectral ratios between pairs of events of Cluster 1, both with (a) strong and (b) weak or no source directivity. The superimposed theoretical curves are based on scaling law inferred using pairs with strong and weak directivity separately. The best-fit parameters p and q differing by 4 and 9 per cent, respectively.

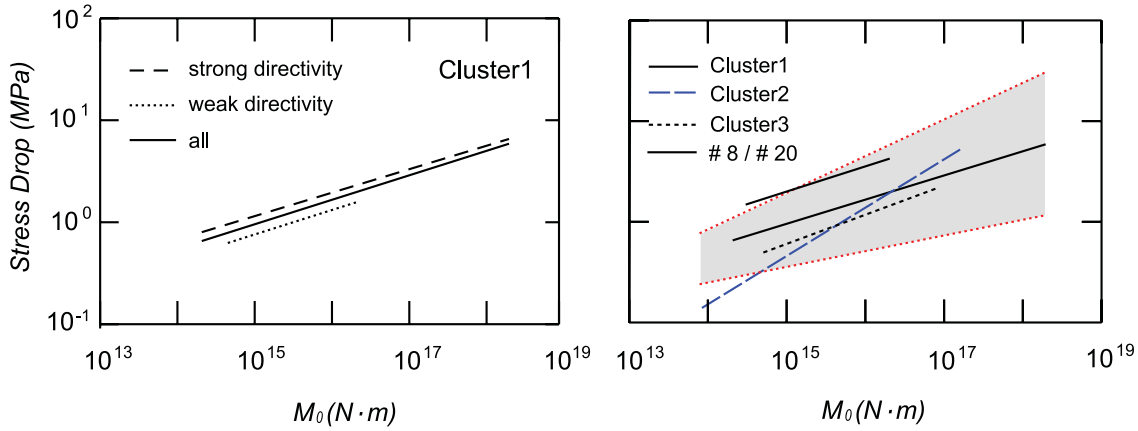

Figure 5. (Left panel) The best-fit solution (eq. 8, black line) of the merged data of weak- and strong-directivity events of Cluster 1 is compared with the solution of the two separate data sets (dashed and dotted lines for strong and weak directivity pairs, respectively). (Right panel) The best-fit solution of the merged three cluster data (thick line) and its estimate uncertainty band (grey area) as inferred from tests of the Appendix. The individual cluster solutions are also shown. The thin line represents the trend of the two reference events used in Section 5.2.

and EGF events; otherwise the variations at individual stations can be very large.

Finally, we repeated the best-fit grid-search procedure using the selected events of the other two clusters (see Table 3). The results are:

$$\begin{aligned} p &= 0.48 \\ q &= -7.5 \end{aligned} \tag{9}$$

for Cluster 2, and

$$\begin{aligned} p &= 0.29 \\ q &= -4.6 \end{aligned} \tag{10}$$

for Cluster 3. Eq. (10), which has been derived from a significant number (84) of spectral ratios, yields a similar trend as Cluster 1 whereas the difference increases for Cluster 2, probably because of the limited number of EGFs. Moreover, event # 16 was deeper than the nearby aftershocks used as EGFs (see Table 1), which can be a further source of error in (9). The similar trend of Cluster 1 and Cluster 3 indicates that stress drops did not change between the clusters, suggesting that all data of Table 1 can be merged. The validity of this choice is confirmed *a posteriori* by the similar behaviour of individual-event stress drops (discussed in Section 5.2). The result, when all the data of the three clusters are merged, is

$$\begin{aligned} p &= 0.26 \\ q &= -4.0. \end{aligned} \tag{11}$$

As mentioned before, to estimate the size of statistical uncertainties, a bootstrap analysis has been applied to the spectral ratio ensemble of the three clusters, by randomly replacing 50 per cent of the original sample with replacements chosen randomly from the original set of ratios. The resulting error was 11 per cent for p and 15 per cent for q that are definitely smaller than the individual spectral-ratio errors which can reach 40 per cent when f_0 approaches the frequency band limit (this estimate is discussed in the Appendix). To be more conservative, we have adopted the latter in Fig 5(b).

To check the statistical significance of the superiority of the varying stress-drop model (11), we have computed the minimum misfit solution when a constant stress-drop model is assumed, that is, by putting $p = 0$ in eq. (6). The quality of the best-fit constant stress-drop model is definitely worse compared to (11) as the misfit increases by 38 per cent: it is $\varepsilon = 0.022$ for the constant $\Delta\sigma$ model against $\varepsilon = 0.016$ that is found when both p and q are free to vary. Moreover, the resulting constant stress drop of the entire data set would be 20 MPa, a value that is larger than the reported estimates of the largest shocks. Fig. 6 compares the trends for some pairs of events. We observe that both constant and varying stress-drop models converge correctly to the same low- and high-frequency asymptotes, the difference, therefore, results from the spectral ratios at intermediate frequencies. The statistically significant difference in the minimum misfit for the varying and constant stress-drop scaling suggests that the available data sample is well suited to constrain the best scaling model irrespective of source directivity. This is confirmed from Figs 6(a) and (b) which shows that the quality of fit of the two models is the same for both weak and strong directivity pairs.

5.2 Individual-event stress drops determined from station spectral ratios

Eq. (11) depicts a well-constrained trend of stress drop to decrease for smaller shocks. However, *a priori* we do not know to what extent the values of individual events deviate from the mean linear fit. Another limitation of the analysis in Section 5.1 is the small number (26) of events which results from the strict criteria imposed in the selection of the EGFs: the target and EGF events must be less than 10 km apart, while the source-to-receiver distance must be $\gg$10 km. To overcome these two limitations, we have considered all the earthquakes analysed by HMM11 that were characterized by a consistent normal-faulting focal mechanism, for a total number of 64 events (Table 2). The assumption of a similar source-to-receiver propagation for pairs of events is still valid since the interdistance between the events, on the average, is one order of magnitude smaller than source-to-receiver distance. Note that, in principle, the spectral ratio (5) can be applied to earthquake pairs independently of their location if propagation can be satisfactorily corrected. In our spectral ratios, the small difference in propagation between numerator and denominator events is compensated through a $1/R$ correction. This correction assumes that the seismograms are mostly dominated by body waves at high frequency. However, the distance ratio is close to 1 and $1/R$ correction does not differ substantially from $1/\sqrt{R}$ that would be required for surface waves.

Spectral ratio (5) defines the ratio of the stress drops of numerator and denominator events (see Fig. S1, panel b) since seismic moments are known *a priori* from HMM11. Therefore, the ratio of $\Delta\sigma$ for different event pairs is a robust indicator of the validity of constant or varying stress-drop scaling. The plot of the $\Delta\sigma$ ratios would depict a flat, scattered trend as a function of the magnitude difference between the pair events if self-similarity holds. However, as Fig. 7(a) shows, this is not the case for L'Aquila earthquakes

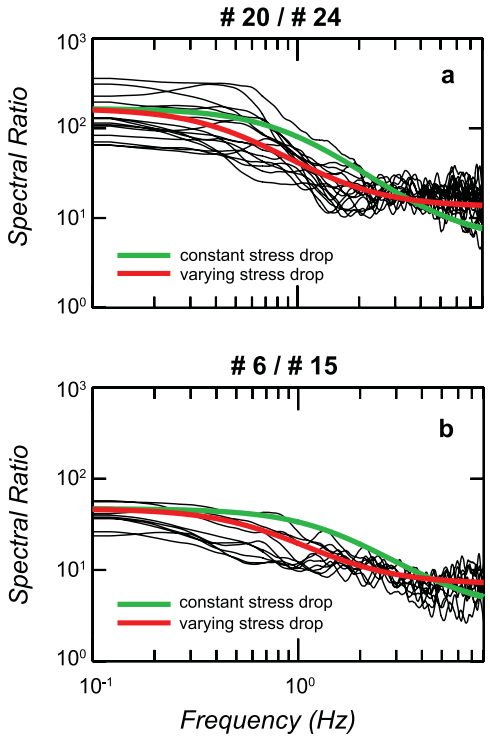

Figure 6. Panels (a) and (b) compare observations with theoretical curves for strong and weak directivity pairs, respectively. The two theoretical curves represent the best constant stress-drop model (in green) and the best-fit model with no *a priori* constraint on stress drop (in red). Misfit is improved by about 40 per cent when stress drop can vary as a function of earthquake size. The two models fit the low- and high-frequency asymptotes equally well, indicating that the intermediate frequency band makes the difference in terms of misfit between constant and varying stress-drop models.

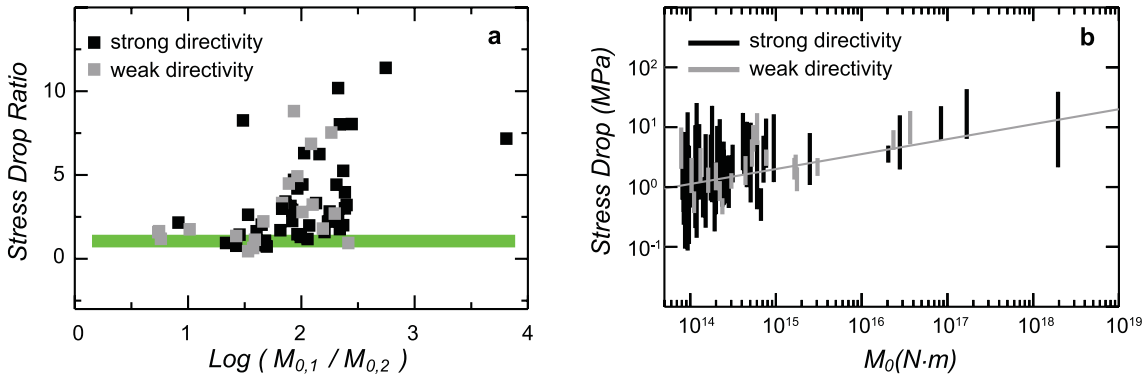

Figure 7. (a) Ratio of stress drop as a function of seismic moment ratio. The expected ratio is 1 (shown by thick horizontal line) for constant stress-drop scaling. There is a clear increase in the stress-drop ratio as the moment ratio increases, confirming the validity of the increasing stress-drop model. (b) Individual-event stress drop estimated from ratio of panel (a) when events # 8 and 20 of Table 2 are used as reference. The choice of this reference event is motivated by its similar $\Delta\sigma$ value in this study and in Ameri *et al.* (2011). The trend of eq. (12) is also superimposed. Both in (a) and (b) no difference emerges in the trend of strong and weak directivity events when the stress-drop average of each event is computed over the available station azimuths.

(the thick horizontal line is the expected trend for the constant stress-drop scaling). The ratio of $\Delta\sigma$ increases monotonically as the seismic moment difference between numerator and denominator increases, depicting an increasing trend. This figure confirms, for all the earthquakes with available independent seismic moment estimate, that a constant stress-drop model fits observations less adequately than an increasing stress-drop model. In Fig. 7(a) we used as reference earthquakes the smallest and the largest event of the L'Aquila sequence with no directivity (listed as # 8 and # 20 in Table 2, see also Fig. S4). Their spectral ratio is consistent with the inferred stress-drop scaling: p and q computed from their spectral ratio are

$$p = 0.25 \quad q = -3.5 \tag{12}$$

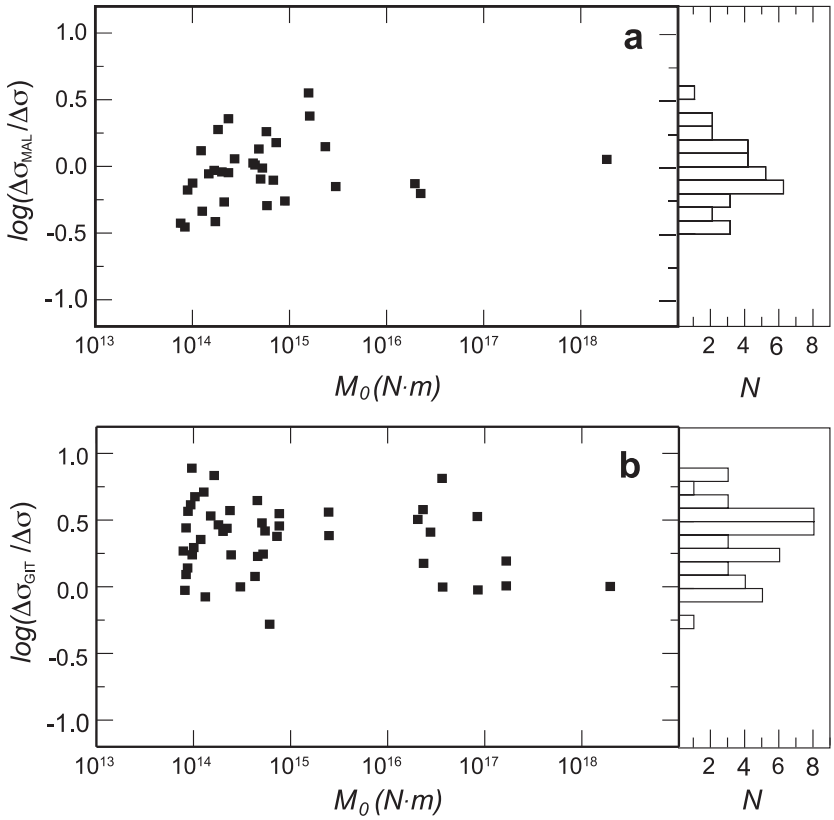

Figure 8. (a) Log ($\Delta\sigma_{MAL}/\Delta\sigma$) as a function of M_0, where $\Delta\sigma_{MAL}$ is stress drop reported by MAL11 or L. Malagnini (personal communication, 2012), and $\Delta\sigma$ is the stress drop of the same event determined in this study (Table 2). All estimates of the stress drop are based on the EGF technique. The ratio is close to 1 for larger events. Although the dispersion in the ratio increases at smaller magnitudes, it never exceeds a factor of 3. The histogram, shown on the right, is centred around the ratio of 1. (b) Log ($\Delta\sigma_{GIT}/\Delta\sigma$) as a function of M_0, where $\Delta\sigma_{GIT}$ is stress drop reported in BIN09 and AME11 using the GIT. Again, $\Delta\sigma$ is the stress drop of the same event determined in this study (Table 2). GIT stress drops show a large and systematic difference with respect to ours at smaller magnitudes; only events with $M_W > 4.5$ the estimates are consistent. The histogram is not centred around 1, indicating a systematic bias between EGF and GIT, up to a factor of 10, with larger values derived from GIT.

and fall within the assessed statistical uncertainties of (11), as shown in Fig. 5(b).

From the stress-drop ratios in Fig. 7(a) we can estimate $\Delta\sigma$ of individual events, when a reference value is fixed. The spectral ratio between event # 8 and # 20 yields $\Delta\sigma = 3.5$ and 1.3 MPa, respectively, if eq. (12) is applied. The stress drop of event # 20 is the same in AME11. Based on the consistency of this value among different studies, we fixed $\Delta\sigma = 1.3$ MPa of this earthquake as a reference and computed $\Delta\sigma$ of all earthquakes listed in Table 2 (Fig. 7b). The largest magnitude earthquakes attain $\Delta\sigma$ values close to 10 MPa, consistent with results from BIN09 and MAL11; for the smallest magnitude events $\Delta\sigma$ decrease to about 1 MPa, on the average, confirming the one-fourth power law of stress drop versus seismic moment inferred in Section 5.1. Note that the results in Fig. 7(b) has been obtained in a completely independent way compared to those of Section 5.1. The same trend $M_0^{0.25}$ was found by Mayeda & Walter (1996) for the Orowan stress drop of earthquakes in western United States and is also consistent with results by Abercrombie & Rice (2005).

As noted by Ben-Zion & Zhu (2002) and simulated by Ben-Zion *et al.* (2003), small earthquakes are likely to propagate in a strongly heterogeneous stress field that prevent them from growing to a larger size, while large earthquakes occur when the stress field is relatively smooth and correlated over large distances. During earthquake failure, the slip increases with rupture dimension considerably less in a strongly heterogeneous stress field than it does in a relatively homogenous stress (Fisher *et al.* 1997; Ben-Zion 2008). Since the stress drop on a given rupture area correlates with the amount of slip, this may explain the increasing stress drops with event size that is observed in this work.

6 DISCUSSION

The variability of $\Delta\sigma$ in Fig. 7(b) is small ($0.5 < \Delta\sigma < 10$ MPa) compared to other studies (e.g. AME11 find $0.1 < \Delta\sigma < 60$ MPa), and indicates a mean tendency to lower values at smaller magnitudes, consistent with the previous results of Section 5.1 (eqs 8, 10 and 11). For comparison, we plotted the difference between our estimates and those by other authors as a function of earthquake size (Fig. 8). In Fig. 8(a) we compare our estimates with those by Malagnini (MAL11 and other unpublished results). Recall that both our estimates and those by Malagnini follow from the application of the EGF technique in the frequency domain, differing only in windowing and smoothing. The figure shows a consistency of estimates over the entire seismic moment range (the histogram is peaked at zero difference), with individual-event stress drops that differ by no more than a factor of 3 between the two groups. In contrast, the comparison with GIT estimates (BIN09 and AME11) in Fig. 8(b) reveals a large difference at smaller magnitudes: the estimated stress drops are consistent only for events with $M_W > 4.5$. Interestingly, the histogram of the lower panel is not centred around one, indicating a systematic bias between EGF and GIT, up to a factor of 10, with larger values derived from GIT. To understand the possible origin of the large differences between EGF and GIT, we have plotted observed spectral ratios of common events with large disparity in $\Delta\sigma$. In Fig. 9 we fit observed spectral ratios of representative events with two theoretical curves: the red one is based on M_0 and $\Delta\sigma$ of Table 2 whereas the green one is drawn from the corresponding values obtained by GIT (BIN09 or AME11). The fits in Fig. 9 suggest that large values of $\Delta\sigma$ in GIT often derive from the difficulty of retrieving correct values of M_0 from the same data that were used

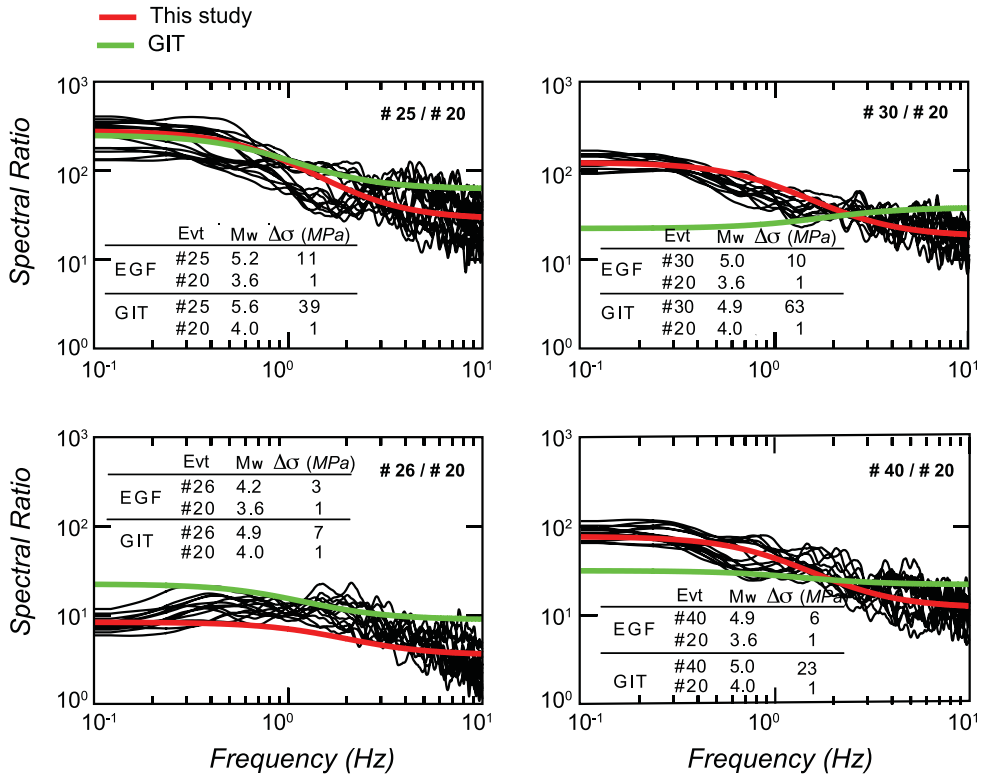

Figure 9. Comparison of observed spectral ratios with theoretical models using EGF and GIT stress drops. Spectral ratios are computed for events whose stress drops obtained from the two methods differ significantly in Fig. 8(b). We find that often unrealistically large values of $\Delta\sigma$ are due to poorly constrained values of M_0 in the GIT studies.

to estimate $\Delta\sigma$ because of the trade-off between these two source parameters. This suggests that independent (very long-period, those by HMM11 were computed for $T > 10$ s) estimates of M_0 should be used to guarantee accurate stress-drop estimates, or alternatively GIT must include constraints based on the low-frequency spectral ratios to avoid errors in seismic moment estimates.

7 CONCLUDING REMARKS

Broad-band seismograms recorded in peninsular Italy during the 2009 L'Aquila seismic sequence illustrate the strong influence that source directivity can have on stress-drop estimates at different azimuths. We think that the need of controlling this effect has been underestimated so far, especially for moderate-to-small magnitude earthquakes. We have demonstrated that ground motion spectra scaled to unitary distance allow the recognition of events with strong source directivity. This information can then be used to minimize the bias of source directivity on stress-drop estimates. The high-frequency asymptote of spectral ratios between large and small events is very sensitive to stress-drop scaling provided that events of similar directivity are used as numerator and denominator. We have found that, in this approach, weak and strong directivity events yield consistent values of stress drops for similar magnitudes and both depict a clear decreasing trend of stress drop towards smaller magnitudes with a factor of 10 variation over four decades of seismic moment, from 1 to 10 MPa in the magnitude range $3.3 \leq M_W \leq 6.1$.

ACKNOWLEDGMENTS

We wish to thank Ingo Grevemeyer (Editor) for his thorough reading of the manuscript and Joe Fletcher and an anonymous reviewer for critical comments and very constructive indications. Yehuda Ben-Zion and Dave Boore gave important suggestions to improve the manuscript. We also thank Jack Boatwright and Paul Spudich for useful discussions. Luca Malagnini made available to us many of his unpublished results, and Gabriele Ameri gave insights on his data set. Daniela Riposati improved the quality of figures.

REFERENCES

Abercrombie, R.E. & Rice, J.R., 2005. Can observations of earthquake scaling constrain slip weakening? *Geophys. J. Int.,* **162,** 406–424.

Akinci, A., Malagnini, L. & Sabetta, F., 2010. Characteristics of the strong ground motions from the 6 April 2009 L'Aquila earthquake, Italy, *Soil Dyn. Earthq. Eng.,* **30,** 320–335.

Ameri, G., Oth, A., Pilz, Bindi, D., Parolai, S., Luzi, L., Mucciarelli, M. & Cultrera, G., 2011. Separation of source and site effects by generalized inversion technique using the aftershock recordings of the 2009 L'Aquila earthquake, *Bull. Earthq. Eng.*, **9,** 717–739.

Anderson, J.G. & Hough, S.E., 1984. A model for the shape of the Fourier amplitude spectrum of acceleration at high frequencies, *Bull. seism. Soc. Am.,* **74,** 1969–1993.

Ben-Zion, Y., 2001. On quantification of the earthquake source, *Seism. Res. Lett.,* **72,** 151–152.

Ben-Zion, Y., 2008. Collective behavior of earthquakes and faults: continuum-discrete transitions, evolutionary changes and corresponding dynamic regimes, *Rev. Geophys.,* **46,** RG4006, doi:10.1029/2008RG000260.

Ben-Zion, Y. & Zhu, L., 2002. Potency-magnitude scaling relations for Southern California earthquakes with $1.0 < M_L < 7.0$, *Geophys. J. Int.,* **148,** F1–F5.

Ben-Zion, Y., Eneva, M. & Liu, Y., 2003. Large earthquake cycles and intermittent criticality on heterogeneous faults due to evolving stress and seismicity, *J. geophys. Res.,* **108**(B6), 2307, doi:10.1029/2002JB002121.

Bindi, D., Pacor, F., Luzi, L., Massa, M. & Ameri, G., 2009. The M_w 6.3, 2009 L'Aquila earthquake: source, path and site effects from spectral analysis of strong motion data, *Geophys. J. Int.,* **179,** 1573–1579.

Boatwright, J., 2007. The persistence of directivity in small earthquakes, *Bull. seism. Soc. Am.,* **97,** 1850–1861.

Boore, D.M., 1986. Short-period P- and S-wave radiation from large earthquakes: implications for spectral scaling relations, *Bull. seism. Soc. Am.,* **76,** 43–64.

Brune, J.N., 1970. Tectonic stress and the spectra of seismic shear waves from earthquakes, *J. geophys. Res.,* **75,** 4997–5009.

Brune, J.N., 1971. Correction (to Brune 1970), *J. geophys. Res.,* **76,** 5002.

Calderoni, G., Rovelli, A., Milana, G. & Valensise, G., 2010. Do strike-slip faults of Molise, central southern Italy, really release a high stress? *Bull. seism. Soc. Am.,* **100,** 307–2324.

Candela, T., Renard, F., Bouchon, M., Schmittbuhl, J. & Brodsky, E.E., 2011. Stress drop during earthquakes: effect of fault roughness scaling, *Bull. seism. Soc. Am.,* **101,** 2369–2387.

Çelebi, M. *et al.*, 2010. Recorded motions of the M_w 6.3 April 6, 2009 L'Aquila (Italy) earthquake and implications for building structural damage: a review, *Earthq. Spectra,* **26,** 651–684.

Chiarabba, C. *et al.*, 2009. The 2009 L'Aquila (central Italy) M_W 6.3 earthquake: main shock and aftershocks, *Geophys. Res. Lett.,* **36,** L18308.

Chioccarelli, E. & Iervolino, I., 2010. Near-source seismic demand and pulse-like records: a discussion for L'Aquila earthquake, *Earthq. Eng. Struct. Dyn.*, **39,** 1039–1062.

Cirella, A., Piatanesi, A., Cocco, M., Tinti, E., Scognamiglio, L., Michelini, A., Lomax, A. & Boschi, E., 2009. Rupture history of the 2009 L'Aquila earthquake from non-linear joint inversion of strong motion and GPS data, *Geophys. Res. Lett.,* **36,** L19304, doi:10.1029/2009GL039795.

Cirella, A., Piatanesi, A., Tinti, E., Chini, M. & Cocco, M., 2012. Complexity of the rupture process during the 2009 L'Aquila, Italy, earthquake, *Geophys. J. Int.*, **190,** 607–621.

Di Alessandro, C., Bonilla, L.F., Boore, D.M., Rovelli, A. & Scotti, O., 2012. Predominant-period site classification for response spectra prediction equations in Italy, *Bull. seism. Soc. Am.,* **102,** 680–695.

Eshelby, J., 1957. The elastic field of an ellipsoid inclusion and related problems, *Proc. R. Soc. Lond.,* **241**(1226), 376–396.

Fisher, D.S., Dahmen, K., Ramanathan, S. & Ben-Zion, Y., 1997. Statistics of earthquakes in simple models of heterogeneous faults, *Phys. Rev. Lett.,* **78,** 4885–4888.

Goldstein, P., Dodge, D., Firpo, M. & Minner, L., 2003. SAC2000: signal processing and analysis tools for seismologists and engineers, in *Invited Contribution to 'The IASPEI International Handbook of Earthquake and Engineering Seismology'*, eds W.H.K. Lee, H. Kanamori, P.C. Jennings & C. Kisslinger, Academic Press, London.

Herrmann, R., Malagnini, L. & Munafò, I., 2011. Regional moment tensors of the 2009 L'Aquila earthquake sequence, *Bull. seism. Soc. Am.,* **101,** doi:10.1785/0120100184.

Keilis-Borok, V., 1959. On estimation of the displacement in an earthquake source and of source dimensions, *Ann. Geofis.*, **12,** 205–214.

Lengliné, O. & Got, J.-L., 2011. Rupture directivity of microearthquake sequences near Parkfield, California, *Geophys. Res. Lett.,* **38,** L08310, doi:10.1029/2011GL047303.

Malagnini, L., Scognamiglio, L., Mercuri, A., Akinci, A. & Mayeda, K., 2008. Strong evidence for non-similar earthquake source scaling in central Italy, *Geophys. Res. Lett.,* **35,** L17303, doi:10.1029/2008GL034310.

Malagnini, L., Akinci, A., Mayeda, K., Munafò, I., Herrmann, R.B. & Mercuri, A., 2011. Characterization of earthquake-induced ground motion from the L'Aquila seismic sequence of 2009, Italy, *Geophys. J. Int.,* **184,** 325–337.

Mayeda, K. & Walter, W.R., 1996. Moment, energy, stress drop, and source spectra of western United States earthquakes from regional coda waves, *J. geophys. Res.,* **101**(B5), 11 195–11 208.

Mayeda, K., Malagnini, L. & Walter, W.R., 2007. A new spectral ratio method using narrow band coda envelopes: evidence for non-selfsimilarity in the Hector Mine sequence, *Geophys. Res. Lett.,* **34,** L11303, doi:10.1029/2007GL030041.

Pino, N.A. & Di Luccio, F., 2009. Source complexity of the 6 April 2009 L'Aquila (central Italy) earthquake and its strongest aftershock revealed by elementary seismological analysis, *Geophys. Res. Lett.,* **36,** L23305, doi:10.1029/2009GL041331.

Rowshandel, B., 2006. Incorporating source rupture characteristics into ground motion hazard analysis models, *Seism. Res. Lett.*, **77,** 708–722

Rowshandel, B., 2010. Directivity Correction for the Next Generation Attenuation (NGA) Relations, *Earthq. Spectra*, **26,** 525–559

Scognamiglio, L., Tinti, E., Michelini, A., Dreger, D., Cirella, A., Cocco, M., Mazza, S. & Piatanesi, A., 2010. Fast determination of moment tensors and rupture history: what has been learned from the 6 April 2009 L'Aquila earthquake sequence, *Seism. Res. Lett.,* **81,** 892–906.

Seekins, L.C. & Boatwright, J., 2010. Rupture directivity of moderate earthquakes in Northern California, *Bull. seism. Soc. Am.,* **100,** 1107–1119.

Singh, S.K., Apsel, R., Fried, J. & Brune, J.N., 1982. Spectral attenuation of SH-waves along Imperial fault, *Bull. seism. Soc. Am.,* **101,** 2003–2016.

Spudich, P. & Chiou, B.S.J., 2008. Directivity in NGA earthquake ground motions: analysis using isochrone theory, *Earthq. Spectra*, **24,** 279–298

APPENDIX: FREQUENCY BANDWIDTH OF SEISMOGRAMS AND ITS EFFECT ON THE ESTIMATION OF STRESS DROP

The spectral ratio (5) is controlled by the ratio of M_0 of numerator and denominator events at low frequency and by the ratio of $M_0^{1/3} \cdot \Delta\sigma^{2/3}$ at high frequency. Thus, the high-frequency asymptote is very sensitive to stress drop and well suited for its estimation (see Fig. S1); the larger the frequency bandwidth the better the $\Delta\sigma$ estimate. Seismic wave propagation in the crust increasingly attenuates high-frequency motions with distance. Seismograms used in this study are recorded at 100–250 km from the source. The signal-to-noise ratio reduces the usable frequency band at these distances. Here we identify the usable frequency bandwidth in our data set and discuss its implications in the accuracy of the stress-drop estimation.

The scaled acceleration spectra to unitary distance (as described in Section 4) easily allow the recognition of noise at high frequencies (Fig. A1). The dominance of noise at high frequency causes the spectral amplitude to deviate from the expected decay due to parameter κ. When the observed spectra are multiplied by $e^{\pi\kappa f}$ to compensate for the high-frequency amplitude diminution due to the attenuation of seismic waves in the crust, the spectral amplitudes increase exponentially above the maximum usable frequency (f_{max}). This effect is easily recognizable, as indicated by the arrows in Fig. A1. We find that, for the data set used in this study,

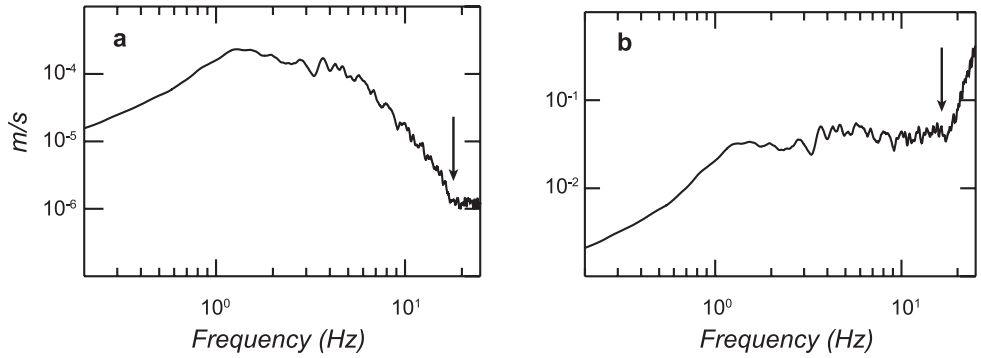

Figure A1. (a) Observed amplitude spectrum of ground acceleration. The flat trend of the spectrum at high frequency (whose beginning is indicated by the arrow) is due the dominance of the noise over signal. (b) The scaled spectrum to unitary distance corrected for attenuation through the term $\exp(\pi\kappa f)$. The amplitude rapidly increases above the frequency where the noise dominates the signal.

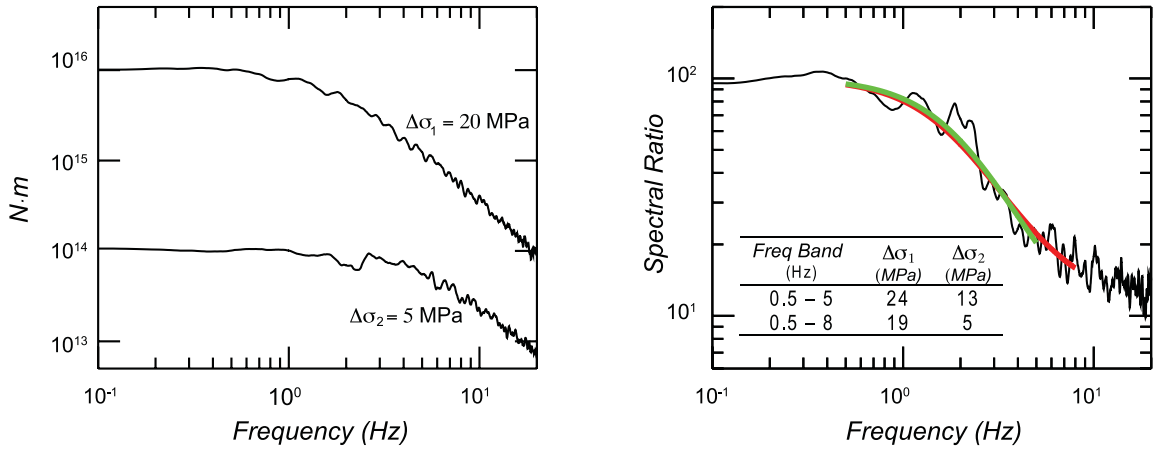

Figure A2. (a) Samples of synthetic displacement spectra. (b) Computed spectral ratios, after the same windowing and smoothing of real seismograms processing (see Fig. A1). The theoretical curves, computed from parameters p and q inferred from the analysis using two different frequency bands are superimposed, and the resulting stress drops are given which may be compared with the theoretical ones shown in (a).

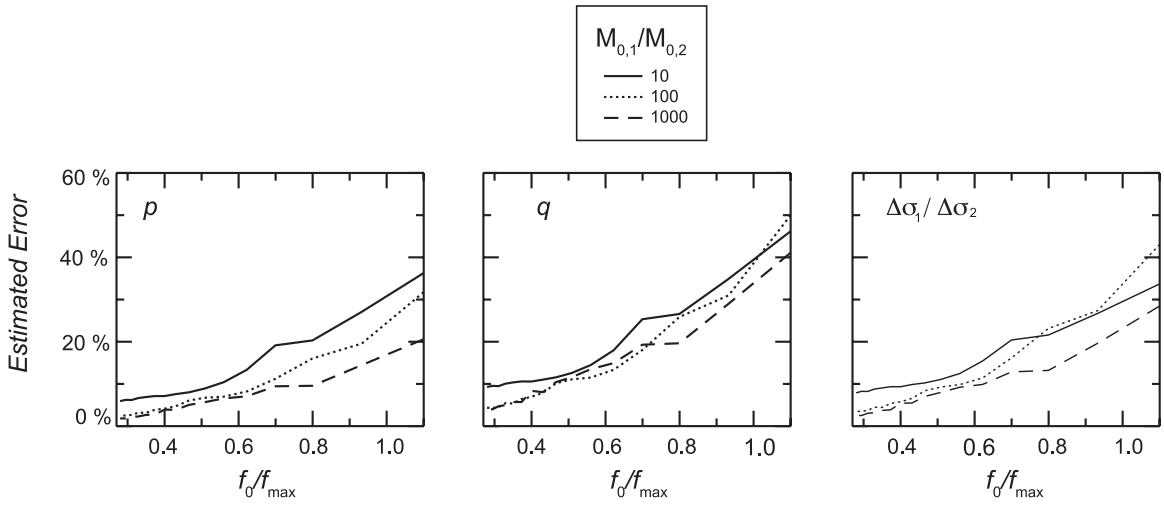

Figure A3. Estimated errors as a function of f_0/f_{max}, where f_0 is the corner frequency of the smaller event and f_{max} is the highest usable frequency unaffected by noise. Errors in p, q and stress-drop ratio are small (<10 per cent) if $f_{max} > 2f_0$, and tend to increase when f_{max} approaches f_0. However, errors do not exceed 50 per cent even for $f_{max} \approx f_0$.

$f_{max} \geq 8$ Hz. Similarly, the noise limits the lowest usable frequency, $f_{min,}$ to 0.5 Hz.

The test of sensitivity of the results on the limited frequency bandwidth is investigated through synthetic spectra. This test is necessary because our method is based on the implicit assumption that the frequency band of analysis is sufficiently broad to include the EGF corner frequency.

Synthetic spectra were generated by using random white-noise time-series (zero mean and unitary standard deviation). These were processed in the same manner as the real seismograms. The white-noise Fourier amplitude spectra were then modulated by theoretical source spectra computed for varying values of M_0 and $\Delta\sigma$. The ratio of seismic moments was varied from 10 to 1000, and the stress drops were varied from 5 to 20 MPa. The corresponding corner frequencies ranged from 0.2 to 5 Hz. Panel (a) of Fig. A2 shows examples of two synthetic spectra. The ratio of synthetic spectra (panel b, Fig. A2) was analysed in the same manner as the real spectra (eqs 4–6). Panel (b) of the figure shows the spectral ratio and theoretical curves computed from parameters p and q inferred from the analysis using two different frequency bands. The resulting stress drops are given in the panel which may be compared with those used in generating the synthetic spectra (panel a).

For each test, 50 simulations were performed using a different seed for each random time-series. This guarantees a satisfactory stability of error estimates. The parameters, estimated from the simulations by applying the minimum misfit criterion (7), were p and q as well as the ratio of stress drops of numerator and denominator events. Tests are repeated for different values of the maximum frequency (f_{max}) at which the analysis is truncated. Fig. A3 shows the estimated errors as function of f_0/f_{max}, where f_0 is the theoretical value of the larger corner frequency of the simulated pair of spectra. The discrepancy between the estimated and imposed values of p and q is illustrated in panels (a) and (b) whereas panel (c) shows the error in the estimated stress-drop ratio. As expected, the figure illustrates the decreasing resolution of the method as f_{max} decreases. However, it can be noted that errors remain acceptable even when f_{max} is of the order of f_0.

SUPPORTING INFORMATION

Additional Supporting Information may be found in the online version of this article:

Figure S1. (a) According to the Brune (1970, 1971) model, which is valid for instantaneous circular crack rupture, the spectral ratio between two earthquakes with seismic moments $M_{0,1}$ and $M_{0,2}$ (similar focal mechanism and hypocentre) is controlled by the difference in seismic moments and corner frequencies (or stress drops, see eq. 5 of the text, and discussion therein). Independently of the station azimuth and distance, the shape of the spectral ratio in the Brune model is characterised by a low-frequency asymptote tending to $M_{0,1}/M_{0,2}$ and a high-frequency asymptote tending to $(M_{0,1}{}^{1/3}\cdot\Delta\sigma_1{}^{2/3})/(M_{0,2}{}^{1/3}\cdot\Delta\sigma_2{}^{2/3})$, where $\Delta\sigma_1$ and $\Delta\sigma_2$ are the stress drops of the numerator and denominator earthquakes. If $\Delta\sigma$ is constant, the high-frequency asymptote must scale as $(M_{0,1}/M_{0,2})^{1/3}$: this constraint may be a powerful tool to check the validity or breakdown of the constant stress-drop scaling over an extended magnitude range. (b) Source directivity causes spectral changes between stations at different source backazimuths (at frequencies $f > f_0$). In this case variations of the high-frequency asymptote of the spectral ratio can be large at stations at different azimuth: these variations become an efficient indicator of source directivity, when one of the two earthquakes has no directivity. The question mark indicates that, at high frequencies, the spectrum slope is expected to change between stations in front and back of the rupture propagation because of energy conservation. In this study we limit our analysis of the spectral ratio splitting to frequencies close to f_0 ($f_{max} = 8$ Hz).

Figure S2. Estimate of the parameter κ of the broad-band stations (see Fig. 1 of the text). Acceleration amplitude spectra are plotted in a lin-log scale, where the linear decay is controlled by $(-\pi\kappa f)$. For each station (two examples are illustrated), the mean κ is computed as the average over the $M_W > 5$ event ensemble using the two horizontal components. The estimate is made in the frequency band (where the thick black straight-line is drawn) that is not affected by corner frequency at low frequency and noise saturation at high frequency. The results are listed above.

Figure S3. Displacement spectra of event pairs with similar source directivity (both with strong directivity on the left-hand side and both with weak directivity on the right-hand side). In both cases, in the individual-station spectral ratios there is no separation in the high-frequency asymptotes as a function of the station azimuth. In distinct contrast, separation between stations at different azimuths may be very large at frequencies $f > f_0$ when numerator and denominator events have different source directivity (in the central panel column).

Figure S4. Individual-station stress drops estimated for a weak directivity event (#47 of Table 2, panel b) and a strong directivity event (#22 of Table 2, panel c) using event # 8 as reference (all station spectra overlap indicating no directivity, panel a). Although theoretical directivity models (Rowshandel 2006, 2010; Spudich & Chiou 2008) predict that the increase of amplitude in front of the rupture propagation is larger than the decrease at stations in the opposite direction, the geometric mean operation for strong directivity events yields results that, at a zero-order approximation, are consistent with those of weak directivity events at similar magnitudes (see Fig. 7 of the text) (http://gji.oxfordjournals.org/lookup/suppl/doi:10.1093/gji/ggs011/-/DC1).